Molecular tuning of CO2-to-ethylene conversion

Fengwang Li, Arnaud Thevenon, Alonso Rosas-Hernández, Ziyun Wang, Yilin Li1, Christine M. Gabardo, Adnan Ozden, Cao Thang Dinh, Jun Li, Yuhang Wang, Jonathan P. Edwards, Yi Xu, Christopher McCallum, Lizhi Tao, Zhi-Qin Liang, Mingchuan Luo, Xue Wang, Huihui Li, Colin P. O'Brien, Chih-Shan Tan, Dae-Hyun Nam, Rafael Quintero-Bermudez, Tao-Tao Zhuang, Yuguang C. Li, Zhiji Han, R. David Britt, David Sinton, Theodor Agapie, Jonas C. Peters & Edward H. Sargent

Version Post-print/Accepted Manuscript

Citation (published version) Li, F., Thevenon, A., Rosas-Hernández, A. *et al.* Molecular tuning of CO2-to-ethylene conversion. *Nature* **577,** 509–513 (2020). https://doi.org/10.1038/s41586-019-1782-2

Molecular tuning of CO_2-to-ethylene conversion

Fengwang Li[1]*, Arnaud Thevenon[2]*, Alonso Rosas-Hernández[2]*, Ziyun Wang[1]*, Yilin Li[1]*, Christine M. Gabardo[3], Adnan Ozden[3], Cao Thang Dinh[1], Jun Li[1,3], Yuhang Wang[1], Jonathan P. Edwards[3], Yi Xu[3], Christopher McCallum[3], Lizhi Tao[4], Zhi-Qin Liang[1], Mingchuan Luo[1], Xue Wang[1], Huihui Li[1], Colin P. O'Brien[3], Chih-Shan Tan[1], Dae-Hyun Nam[1], Rafael Quintero-Bermudez[1], Tao-Tao Zhuang[1], Yuguang C. Li[1], Zhiji Han[2], R. David Britt[4], David Sinton[3], Theodor Agapie[2], Jonas C. Peters[2], Edward H. Sargent[1]

[1]Department of Electrical and Computer Engineering, University of Toronto, 35 St George Street, Toronto, Ontario M5S 1A4, Canada

[2]Division of Chemistry and Chemical Engineering, California Institute of Technology, Pasadena, California 91125, USA

[3]Department of Mechanical and Industrial Engineering, University of Toronto, 5 King's College Road, Toronto, Ontario, M5S 3G8, Canada

[4]Department of Chemistry, University of California, Davis, California 95616, USA

*These authors contributed equally to this work.

The electrocatalytic CO_2 reduction reaction (CO_2RR) to value-added fuels and feedstocks provides a sustainable and carbon-neutral approach to the storage of intermittent renewable electricity[1]. The highly selective generation of economically desirable C_2 products such as ethylene from CO_2RR remains a challenge[2]. Tuning the stabilities of intermediates to favor a desired reaction pathway offers the opportunity to enhance selectivity[3-5], and this has recently been explored on copper (Cu) via control over morphology[6], grain boundaries[7], facets[8], oxidation state[9], and dopants[10]. Unfortunately, the faradaic efficiency (FE) for ethylene is still low in neutral media (60% at a partial current density of 7 mA cm^{-2} in the best catalyst reported so far[9]), resulting in a low energy efficiency (EE). Here we present a molecular tuning strategy – the functionalization of the surface of electrocatalysts with organic molecules – that stabilizes intermediates for enhanced CO_2RR to ethylene. We investigate – using electrochemical, *operando* / *in situ* spectroscopic, as well as computational, studies – the influence of a library of molecules, derived via electro-dimerization of arylpyridiniums[11], on Cu. We find that the adhered molecules improve the stabilization of an *atop*-bound CO intermediate, thereby favoring further reduction to ethylene. As a result of this strategy, we report the CO_2RR to ethylene with an FE of 72% at a partial current density of 230 mA cm^{-2} in a liquid-electrolyte flow cell in neutral medium. We report stable ethylene electrosynthesis for 190 hours in a membrane electrode assembly (MEA) based system that provides a full-cell EE of 20%. These findings indicate how molecular strategies can complement heterogeneous catalysts by stabilizing intermediates via local molecular tuning.

Recently we found that an *N*-aryl-substituted tetrahydro-4,4'-bipyridine organic thin film, formed via reductive electro-dimerization of an *N*-aryl pyridinium additive (Fig. 1a, see Methods in Supplementary Information for details), facilitated selective CO_2RR to multi-

carbon products on Cu foils[11]. However, the selectivity and partial current density for ethylene are low (~40% and 0.5 mA cm^{-2}) for practical applications. We sought to clarify factors contributing to the selectivity enhancement to enable further design of new functional molecules with better performance.

Noting that local environment plays a role in electrocatalysis through tuning interactions among reactants/intermediates[12-16], we postulated that the *N*-arylpyridinium-derived film may affect the selectivity of CO_2RR by interacting with the reaction intermediate(s). To test this hypothesis, we first prepared a library of *N*-arylpyridinium salts (**1**–**11**, Fig. 1b, Supplementary Figs. 1 and 2) expected to display different electronic properties. We then electrodeposited these *N*-arylpyridinium precursors onto a porous polytetrafluoroethylene (PTFE) electrode[17] with a sputtered Cu layer serving as both current collector and catalyst. The as-electrodeposited thin film is water-insoluble and consists of a mixture of both constitutional and stereo isomers of *N*-aryl-substituted tetrahydro-bipyridine species (Fig. 1a, Supplementary Note 1, Supplementary Figs. 3–5). As expected, Bader charge analysis points to different electron donating abilities of these tetrahydro-bipyridines (Supplementary Fig. 6). Coating of the tetrahydro-bipyridine film onto the Cu electrode does not change substantially its morphology, crystallinity, electronics and wettability, nor does it retard the transport of reactants, ions and products, needed in electrocatalytic processes (Supplementary Note 2, Supplementary Figs. 7–10).

We evaluated CO_2RR properties of these tetrahydro-bipyridine-functionalized electrodes in a liquid-electrolyte flow cell system (Supplementary Fig. 11) using CO_2-saturated 1 molar aqueous $KHCO_3$ as the supporting electrolyte. In this system, the abundant catalyst/electrolyte/CO_2 triple-phase interfaces overcome the CO_2 mass-transport limit[17,18], and thus enable commercially relevant current densities[19,20]. We note that, though the large

achievable current densities in the flow cell drive up local pH (Supplementary Fig. 12), the tetrahydro-bipyridine layer does not create a further pH gradient near the active Cu surface (Supplementary Note 2). The layer is chemically robust to the locally alkaline environment (Supplementary Fig. 13). The FE for ethylene (Supplementary Table 1) on additive-modified Cu-**x** electrodes (**x = 1–11**), at the optimal applied potentials, -0.82 V – -0.84 V *vs.* the reversible hydrogen electrode (RHE, all potentials are with respect to this reference), was plotted against the Bader charge of the nitrogen atom of each tetrahydro-bipyridine structure (Fig. 1c). We found a volcano-shaped trend relating FE and Bader charge, with the tetrahydro-bipyridine of moderate electron donating ability showing the highest ethylene selectivity.

We further found a volcano-shaped relationship between the ethylene selectivity and the ratio of *atop* bound CO (CO_{atop}) to *bridge* bound CO (CO_{bridge}) on Cu-**x** surfaces (Fig. 2a). We identified and quantified these bound CO configurations through *in situ* Raman spectroscopic interrogation[21-24] of these surfaces (Supplementary Note 3, Supplementary Figs. 14 and 15, Supplementary Table 2). In all cases, the ratio of CO_{atop} to CO_{bridge} on Cu-**x** was increased compared to that on bare Cu. Noting a correlation between ethylene selectivity and electron-donation propensity (Fig. 1c), we hypothesized that the change of the relative population of CO_{atop} and CO_{bridge} could arise from the difference in electron-donating abilities of the tetrahydro-bipyridines. Indeed, we found that the ratio of CO_{atop} to CO_{bridge} was positively correlated with the Bader charge of the nitrogen atom in the tetrahydro-bipyridines (Fig. 2b). This finding suggests that electron donation to the *CO stabilizes the *atop* CO more significantly than it does the *bridge* CO.

To gain molecular level insight into the effect of CO binding, we calculated, using density functional theory (DFT), reaction barriers for the CO dimerization step, a critical step along the pathway to C_2 products[5], on Cu(111) with the initial configurations of two *CO on the

atop:*atop*, *atop*:*bridge*, and *bridge*:*bridge* sites (Fig. 2c, Supplementary Fig. 16). We found the lowest barrier of CO dimerization to be at the *atop*:*bridge* site with a barrier of 0.72 eV. In comparison, the barrier for the *bridge*:*bridge* site is 0.82 eV. The barrier for the *atop*:*atop* site could not be identified: one of the CO on *atop* site tends to relocate to *bridge* site, suggesting that *atop*:*atop* is not favorable for CO dimerization. These findings indicate that neither too large nor too small of a population of *atop* CO favors C_2 selectivity.

We further calculated the adsorption of CO on Cu(111) (Supplementary Fig. 17, Supplementary Table 3). On bare Cu(111), the *bridge* site appears to be the most stable adsorption site for CO. In the presence of the tetrahydro-bipyridine formed from **1**, the adsorption of CO on both *bridge* and especially *atop* sites is enhanced and the *atop* site becomes favored compared to the *bridge* site. The enhancement of CO binding energy decreases the desorption of *CO and increases the likelihood of further reduction of *CO to ethylene (Supplementary Figs. 18–20).

We visualized the interaction between the tetrahydro-bipyridine molecule and *CO through the electron density difference plot (Fig. 2d). The electron density appears to transfer from the molecule to nearby water molecules, changing the electronic distributions of water surrounding *CO, and enhancing CO adsorption in the favorable *atop* site.

In sum, our working model is that H_2O-mediated electron density transfer of the tetrahydro-bipyridine film to *CO stabilizes this intermediate, especially on the *atop* site, and therefore promotes the energy-favorable dimerization of *bridge*:*atop* bound CO, leading to enhanced ethylene selectivity. However, too strong adsorption of CO caused by strong electron donation of some tetrahydro-bipyridines (right side of the volcano plot in Fig. 1c) results in overload of *atop*-bound CO and thus yields energy barriers too large for further reaction.

We found, using *operando* X-ray absorption spectroscopy (Supplementary Fig. 21), that tetrahydro-bipyridine does not modulate the oxidation state or coordination environment of Cu – though such modulation is known to promote ethylene formation[9,25]. We also found, via *in situ* electrochemical electron paramagnetic resonance spectroscopic and isotopic labeling studies (Supplementary Figs. 22–24), that tetrahydro-bipyridine does not mediate electron transfers via its conversion to pyridinium radicals[16,26], nor does it mediate hydrogen transfers steps.

Since the nitrogen atom of the *N*-aryl-substituted pyridine ring influences the binding of *CO, we posited that an *N*-aryl-pyridinium-derived molecule with more nitrogen sites and optimal electron donating properties would stabilize more *CO on the Cu surface. Accordingly, we synthesized an *N*,*N*'-(1,4-phenylene)bispyridinium salt (**12**, Fig. 3a, Supplementary Fig. 1). In contrast with **1**–**11**, **12** underwent oligomerization to form an *N*-aryl-dihydropyridine-based oligomer under electrodeposition (Fig. 3a, Supplementary Fig. 5). The Bader charge of the nitrogen atom of the oligomer (Supplementary Fig. 6) is close to that of the tetrahydro-bipyridine from **1**, and, as expected, the ratio of CO_{atop} to CO_{bridge} on Cu-**12** (Supplementary Fig. 15, Supplementary Table 2) is also close to that on Cu-**1**. Based on the working hypotheses presented herein, these findings suggest the Cu-**12** catalyst should approach the top of the volcano plot.

We evaluated the CO_2RR performance of Cu-**12** in the same flow cell system. The ethylene FE on Cu-**12** is higher than that on bare Cu and other Cu-**x** across the entire applied potential range (-0.49 – -0.84 V) and achieves the peak value of 72% at -0.83 V (Fig. 3b, Supplementary Tables 1 and 4). This is the highest selectivity for ethylene reported in neutral media (Supplementary Table 5). In contrast, the ethylene FE on bare Cu under similar conditions is below 40%. High

selectivity and high current density combine for an ethylene production current of 232 mA cm^{-2} at -0.83 V (Supplementary Fig. 25).

We examined the FEs of CO and ethylene across the applied potential range. Although the FE of CO follows the same trend of peaking at moderate potentials, more CO is converted to ethylene on Cu-**12** compared to on pure Cu (Fig. 3c, Supplementary Table 4). Specifically, at the applied potential of -0.83 V, the FEs of CO and ethylene on Cu-**12** electrode are 5% and 72%, respectively, while the values on bare Cu are 35% and 37%, respectively (Supplementary Fig. 25). The FEs of other CO_2RR products remain similar on both catalysts. These findings suggest that the increased ethylene selectivity arises primarily at the expense of CO evolution. This behavior agrees with the *in situ* Raman spectroscopy and DFT calculations, where the *CO is well-stabilized for ongoing reduction on the molecularly-functionalized Cu electrode. We confirmed via isotopic CO_2 studies (Supplementary Fig. 26) that the products were from CO_2RR.

To evaluate the potential of the Cu-**12** catalyst for practical applications, we integrated it into a MEA device (Supplementary Note 4, Supplementary Figs. 27–34) for electrosynthesis of ethylene via the overall reaction:

$$2CO_2 + 2H_2O \rightarrow C_2H_4 + 3O_2 \qquad E^\circ = 1.15\ V$$

We operated the MEA system at a full-cell voltage of 3.65 V for 190 hours. It exhibited a stable current (~600 mA) and a stable ethylene selectivity (64%) in neutral medium (Fig. 4). The EE of the system is determined to be 20% via:

$$EE_{full\ cell} = E^\circ \times FE_{ethylene} \div E_{full\ cell}$$

Overall, this work presents a strategy to tune the stabilization of intermediates on heterogeneous electrocatalysts via the introduction of molecules. Using this strategy, implemented using *N*-aryl-substituted tetrahydro-bipyridine films and a related oligomeric film

on a Cu catalyst, we achieved the CO_2-to-ethylene conversion with an ethylene FE of 72% and a full-cell EE of 20% in neutral media. In light of this performance, in combination with the long-term operating stability, the strategy indicates a promising platform for the CO_2 conversion into value-added chemicals using renewable electricity.

Reference

1 Seh, Z. W. et al. Combining theory and experiment in electrocatalysis: insights into materials design. *Science* **355**, eaad4998 (2017).

2 De Luna, P. et al. What would it take for renewably powered electrosynthesis to displace petrochemical processes? *Science* **364**, eaav3506 (2019).

3 Li, Y. & Sun, Q. Recent advances in breaking scaling relations for effective electrochemical conversion of CO_2. *Adv. Energy Mater.* **6**, 1600463 (2016).

4 Calle-Vallejo, F. & Koper, M. T. Theoretical considerations on the electroreduction of CO to C_2 species on Cu(100) electrodes. *Angew. Chem. Int. Ed.* **52**, 7282-7285 (2013).

5 Montoya, J. H., Shi, C., Chan, K. & Nørskov, J. K. Theoretical insights into a CO dimerization mechanism in CO_2 electroreduction. *J. Phys. Chem. Lett.* **6**, 2032-2037 (2015).

6 Yang, K. D. et al. Morphology-directed selective production of ethylene or ethane from CO_2 on a Cu mesopore electrode. *Angew. Chem. Int. Ed.* **56**, 796-800 (2017).

7 Li, C. W., Ciston, J. & Kanan, M. W. Electroreduction of carbon monoxide to liquid fuel on oxide-derived nanocrystalline copper. *Nature* **508**, 504-507 (2014).

8 Jiang, K. et al. Metal ion cycling of Cu foil for selective C-C coupling in electrochemical CO_2 reduction. *Nat. Catal.* **1**, 111-119 (2018).

9 Mistry, H. et al. Highly selective plasma-activated copper catalysts for carbon dioxide reduction to ethylene. *Nat. Commun.* **7**, 12123 (2016).

10 Zhou, Y. et al. Dopant-induced electron localization drives CO_2 reduction to C_2 hydrocarbons. *Nat. Chem.* **10**, 974-980 (2018).

11 Han, Z., Kortlever, R., Chen, H. Y., Peters, J. C. & Agapie, T. CO_2 reduction selective for $C_{\geq 2}$ products on polycrystalline copper with N-substituted pyridinium additives. *ACS Cent. Sci.* **3**, 853-859 (2017).

12 Rosen, B. A. et al. Ionic liquid-mediated selective conversion of CO_2 to CO at low overpotentials. *Science* **334**, 643-644 (2011).

13 Masel, R. I. & Rosen, B. A. Catalyst mixtures. US patent 8956990 (2015).

14 Masel, R. I. & Rosen, B. A. Electrochemical devices comprising novel catalyst mixtures. US patent 9464359 (2016).

15 Masel, R. I. & Rosen, B. A. Catalyst mixtures. US patent 9566574 (2017).

16 Cole, E. B. et al. Using a one-electron shuttle for the multielectron reduction of CO_2 to methanol: kinetic, mechanistic, and structural insights. *J. Am. Chem. Soc.* **132**, 11539-11551 (2010).

17 Dinh, C.-T. et al. CO_2 electroreduction to ethylene via hydroxide-mediated copper catalysis at an abrupt interface. *Science* **360**, 783-787 (2018).

18 Li, J. et al. Efficient electrocatalytic CO_2 reduction on a three-phase interface. *Nat. Catal.* **1**, 592-600 (2018).

19 Ma, S. et al. One-step electrosynthesis of ethylene and ethanol from CO_2 in an alkaline electrolyzer. *J. Power Sources* **301**, 219-228 (2016).

20 Jouny, M., Luc, W. W. & Jiao, F. General techno-economic analysis of CO_2 electrolysis systems. *Ind. Eng. Chem. Res.* **57**, 2165-2177 (2018).

21 Sheppard, N. & Nguyen, T. T. *Advances in Infrared and Raman Spectroscopy*. Vol. 5 67 (Heyden, London, 1978).

22 Gunathunge, C. M. et al. Spectroscopic observation of reversible surface reconstruction of copper electrodes under CO_2 reduction. *J. Phys. Chem. C* **121**, 12337-12344 (2017).

23 Heyes, J., Dunwell, M. & Xu, B. CO_2 reduction on Cu at low overpotentials with surface-enhanced in situ spectroscopy. *J. Phys. Chem. C* **120**, 17334-17341 (2016).

24 Akemann, W. & Otto, A. Vibrational modes of CO adsorbed on disordered copper films. *J. Raman Spectrosc.* **22**, 797-803 (1991).

25 Xiao, H., Goddard, W. A., Cheng, T. & Liu, Y. Cu metal embedded in oxidized matrix catalyst to promote CO_2 activation and CO dimerization for electrochemical reduction of CO_2. *Proc. Natl. Acad. Sci.* **114**, 6685-6688 (2017).

26 Cole, E. B., Sivasankar, N., Parajuli, R. & Keets, K. A. Reducing carbon dioxide to products. US patent 8845878 (2014).

Supplementary Information is linked to the online version of the paper at www.nature.com/nature.

Acknowledgements

This work was financially supported by the Ontario Research Fund: Research Excellence Program, the Natural Sciences and Engineering Research Council (NSERC) of Canada, the CIFAR Bio-Inspired Solar Energy program, and the Joint Centre of Artificial Synthesis, a DOE Energy Innovation Hub, supported through the Office of Science of the U.S. Department of Energy under Award Number DE-SC0004993. All DFT computations were performed on the IBM BlueGene/Q supercomputer with support from the Southern Ontario Smart Computing Innovation Platform (SOSCIP). SOSCIP is funded by the Federal Economic Development Agency of Southern Ontario, the Province of Ontario, IBM Canada Ltd., Ontario Centres of Excellence, Mitacs and 15 Ontario academic member institutions. This research was enabled in part by support provided by Compute Ontario (www.computeontario.ca) and Compute

Canada (www.computecanada.ca). This research used synchrotron resources of the Advanced Photon Source (APS), an Office of Science User Facility operated for the U.S. Department of Energy (DOE) Office of Science by Argonne National Laboratory, and was supported by the U.S. DOE under Contract No. DE-AC02-06CH11357, and the Canadian Light Source and its funding partners. The authors thank Dr. T. Wu and L. Ma for technical support at 9BM beamline of APS. D.S. acknowledges the NSERC E.W.R Steacie Memorial Fellowship. A.T. acknowledges Marie Skłodowska-Curie Fellowship H2020-MSCA-IF-2017 (793471). J.L. acknowledges the Banting postdoctoral fellowship. C.M.G. acknowledges NSERC for funding in the form of a postdoctoral fellowship from the government of Canada. J.P.E. thanks NSERC, Hatch and the Government of Ontario for their support through graduate scholarships.

Author Contributions

E.H.S., T.A. and J.C.P. supervised this project. F.L. and Y.L. carried out electrochemical experiments. A.T. and A.R.H. carried out molecule synthesis and characterizations. Z.W. carried out DFT calculations. C.M.G. and F.L. conducted in situ Raman measurement. F.L. and A.O. carried out the MEA experiments. J. L. and F.L. performed X-ray spectroscopy measurements. Y.W. carried out SEM and EIS measurements. J.P.E. measured the contact angle. C.M. carried out the Comsol modelling. L.T. carried out EPR measurement under the supervision of R.D.B.. M.L. performed part of electrochemical experiments. Z. Q. L., X.W. and H.L. provided help in NMR analysis. C.M.G., C.P.O. and Y.X. provided help in MEA measurements. C.S.T. carried out AFM measurement. D.H.N. conducted XRD measurement. R.Q.B. carried out XPS measurement. C.T.D., T.Z, Y.C.L. and Z.H. provided help in materials synthesis and characterizations. F.L. and E.H.S. wrote the manuscript. All authors discussed the results and assisted during manuscript preparation.

Author Information

Reprints and permissions information is available at www.nature.com/reprints. The authors declare no competing interests. Correspondence and requests for materials should be addressed to Edward H. Sargent (ted.sargent@utoronto.ca), Jonas C. Peters (jpeters@caltech.edu) or Theodor Agapie (agapie@caltech.edu).

Data Availability Statement

The datasets generated during and/or analysed during the current study are available from the corresponding author on reasonable request.

Figure Legends

Fig. 1 | Dimerization of *N*-arylpyridinium additives, and correlation of ethylene selectivity with Bader charge. a, Reaction describing the electro-dimerization process that converts an *N*-arylpyridinium salt to a mixture of *N*-aryl-substituted tetrahydro-bipyridines. **b**, Molecular structures of additives **1**–**11**. **c**, Trend for ethylene FE and calculated Bader charge for the nitrogen atom of the *N*-aryl-substituted tetrahydro-bipyridines prepared from **1**–**11**. Due to the symmetric molecular structure of the tetrahydro-bipyridines, a hydrogen atom was used to replace half of the dimer unit (see Supplementary Fig. 6 for details). A spread of Bader charges for the nitrogen, covering the limiting values of the *para,para* and *ortho,ortho* structures, was plotted. The corresponding error bars for ethylene FE uncertainty were arbitrarily placed in the middle of the interval for those tetrahydro-bipyridines where the *para,para* vs. the *ortho,ortho* ratio could not be reliably determined by ^{1}H NMR spectroscopy. The circles correspond to the average contribution from both the *para,para* and *ortho,ortho* isomers where their ratio could be determined by ^{1}H NMR spectroscopy (see Supplementary Note 1 for details). The error bars for ethylene FE uncertainty represent one standard deviation based on three independent samples.

Fig. 2 | Mechanistic investigations of the stabiliztion of CO-bound intermediates. a, The relationship between the ethylene FE and the ratio of *atop* CO and *bridge* CO on Cu-**x** electrodes. The relative population of these two kinds of Cu-bound CO was calculated through the integrated areas of each band in the Raman spectra, which are proportional to the corresponding *CO coverage (see Supplementary Note 3 for more details). The error bars for ethylene FE uncertainty represent one standard deviation based on three independent samples. **b**, The relationship between the ratio of *atop* CO and *bridge* CO on Cu-**x** and the Bader charge for the nitrogen atom of the *N*-aryl-substituted tetrahydro-bipyridine formed from additive **x**. The Bader charges were calculated using the same protocol as in Fig. 1. The error bars for the ratio of CO_{atop} to CO_{bridge} in **a** and **b** represent one standard deviation based on two independent measurements. **c**, Energy barriers of the dimerization of two CO at both *bridge* sites and two CO at *bridge* and *atop* sites, respectively. IS: initial state, TS: transient state, FS: final state. **d**, Electron density difference plots for the CO adsorption with one water layer and the tetrahydro-bipyridine formed from **1**. The yellow and blue contours represent electron density accumulations and depressions, respectively. Dashed lines indicate hydrogen bond network. Red: O, grey: C, blue: N, white: H, and pink: Cu.

Fig. 3 | CO_2RR performance in liquid-electrolyte flow cells. a, Reaction describing the electro-oligomerization of the *N*,*N*'-(1,4-phenylene)bispyridinium salt **12** to form an *N*-aryl-dihydropyridine-based oligomer. **b**, FE of ethylene on Cu and Cu-**12** using CO_2-saturated 1 molar $KHCO_3$ as the supporting electrolyte. **c**, FEs of CO and ethylene on Cu and Cu-**12** at the applied potential range of -0.47 to -0.84 V. The error bars for FE uncertainty represent one standard deviation based on three independent samples.

Fig. 4 | Ethylene electrosynthesis in a membrane electrode assembly device. Cu-**12** and iridium oxide supported on titanium mesh were used as the cathode and anode, respectively. Humidified CO_2 was flowed through the gas channels in the cathode and 0.1 molar aqueous

$KHCO_3$ solution was flowed through channels in the anode. The anode and cathode were seperated by an anion exchange membrane to form the membrane electrode assembly. The total geometric area of the flow field in the cathode is 5 cm^2, of which 45% is the gas channel while the rest 55% is the land area (Supplementary Figs. 27 and 28). Full-cell voltage was gradually increased from 3 V to 3.65 V and kept constant starting at time = 0.

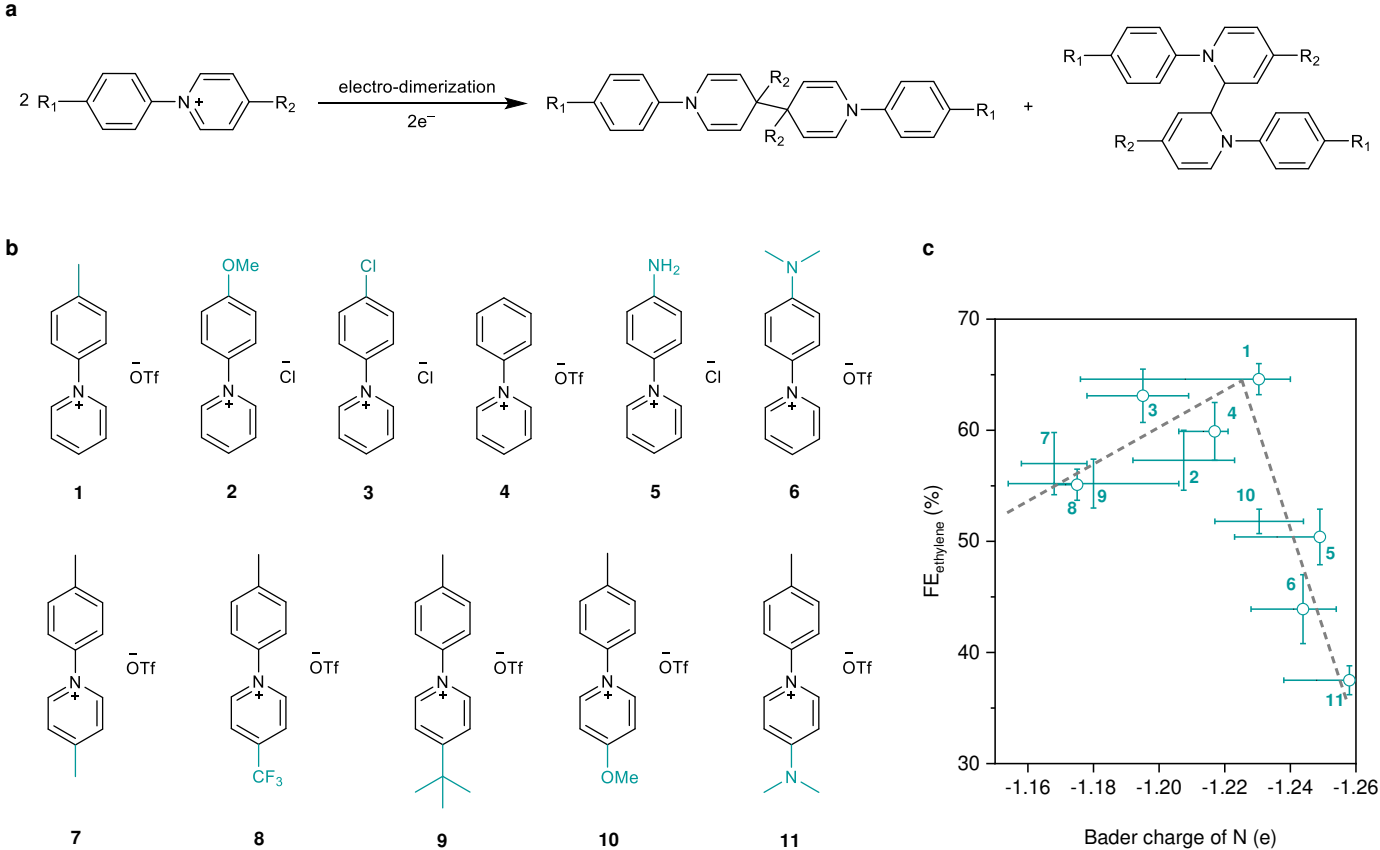
a
2 R1
N+
R2
electro-dimerization
2e−
R1
N
R2
R2
N
R1
+
R1
N
R2
R2
N
R1
b
OTf
OMe
Cl
Cl
OTf
NH2
Cl
N
OTf
1
2
3
4
5
6
OTf
CF3
OTf
OTf
OMe
OTf
N
OTf
7
8
9
10
11
c
70
60
50
40
30
FEethylene (%)
1
3
4
7
2
8
9
10
5
6
11
-1.16
-1.18
-1.20
-1.22
-1.24
-1.26
Bader charge of N (e)

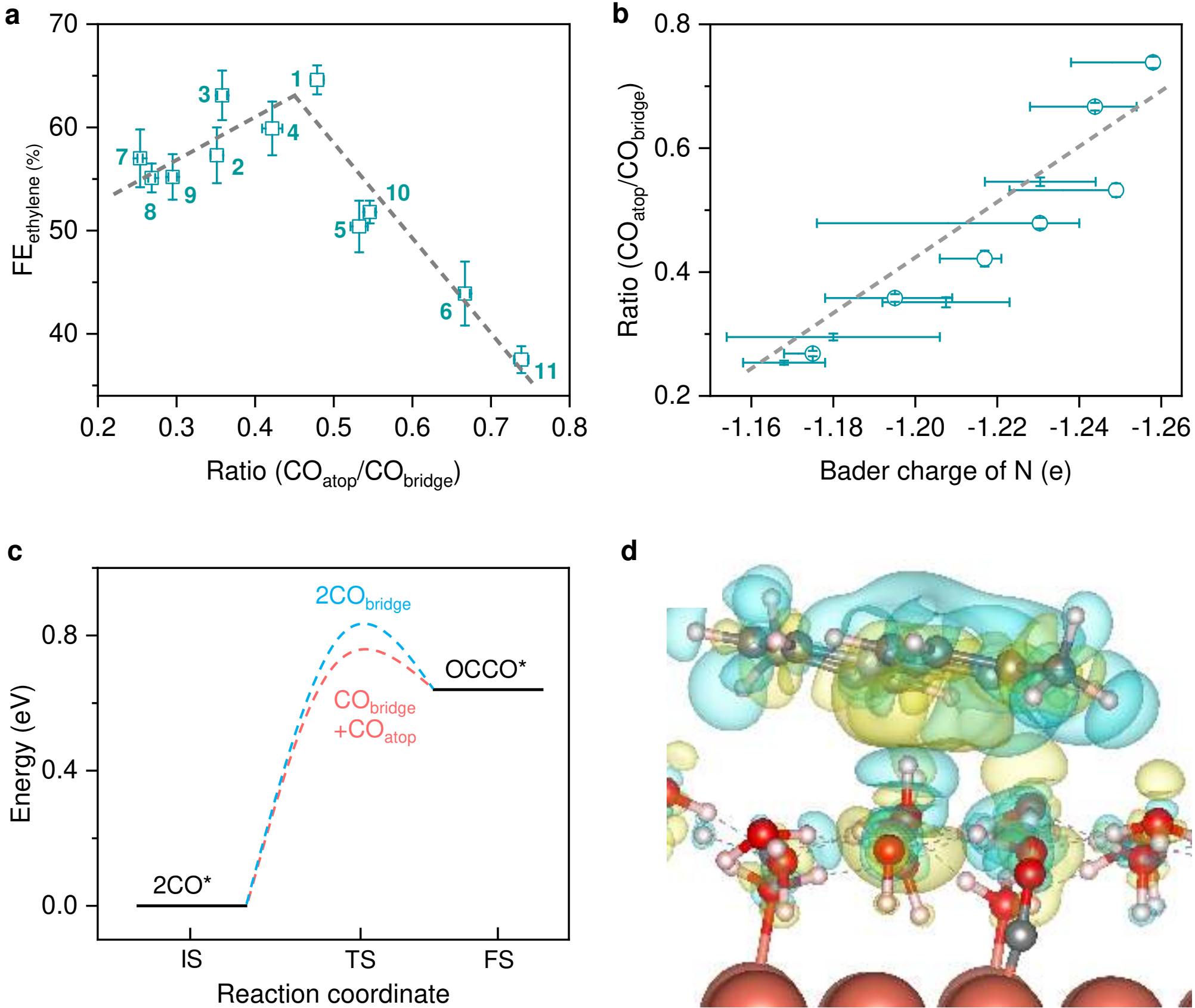
a
70
60
50
40
FE$_{ethylene}$ (%)
0.2
0.3
0.4
0.5
0.6
0.7
0.8
Ratio (CO$_{atop}$/CO$_{bridge}$)
1
2
3
4
5
6
7
8
9
10
11
b
0.8
0.6
0.4
0.2
Ratio (CO$_{atop}$/CO$_{bridge}$)
-1.16
-1.18
-1.20
-1.22
-1.24
-1.26
Bader charge of N (e)
c
2CO$_{bridge}$
OCCO*
CO$_{bridge}$
+CO$_{atop}$
2CO*
0.8
0.4
0.0
Energy (eV)
IS
TS
FS
Reaction coordinate
d

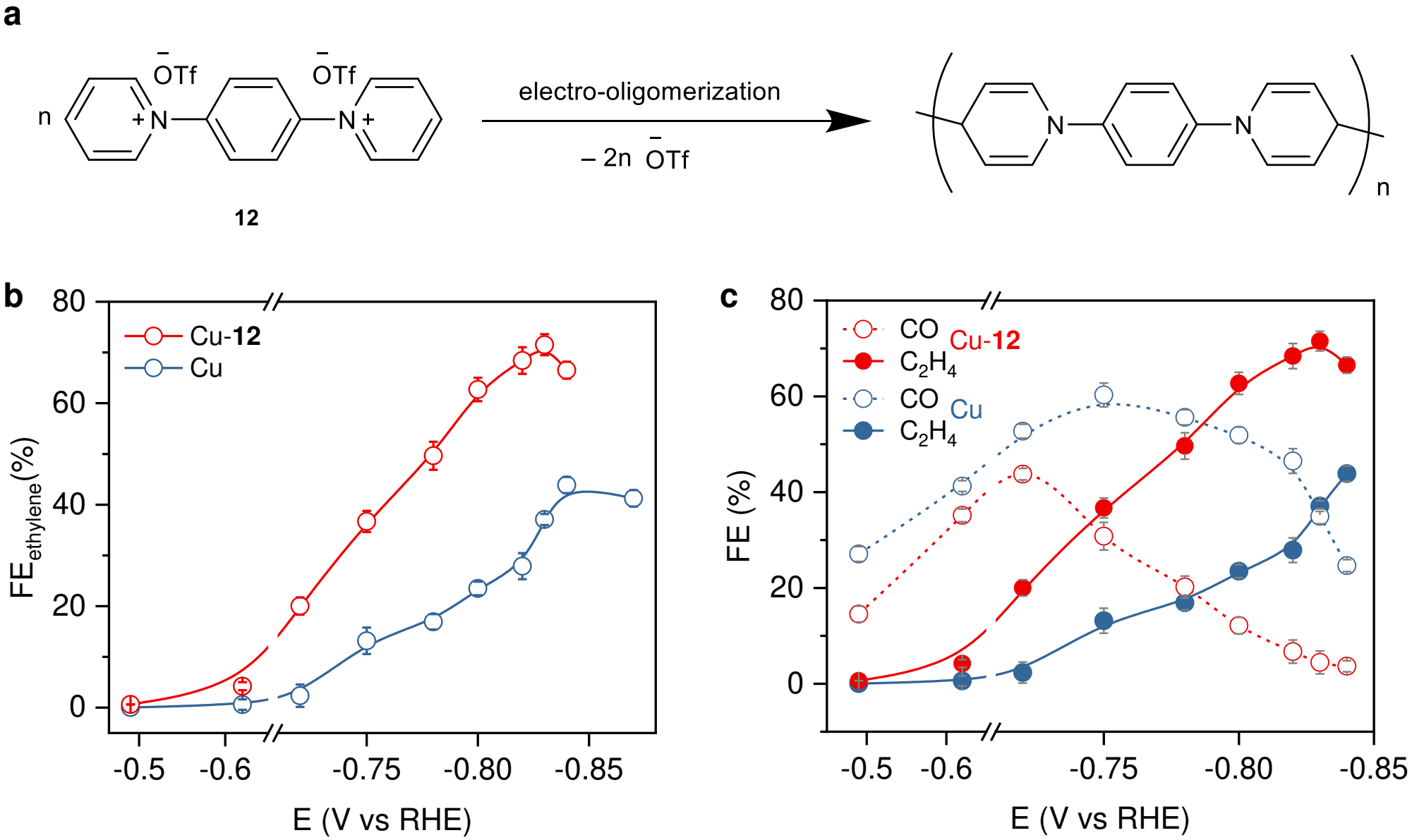
a
n
OTf
OTf
N+
N+
12
electro-oligomerization
– 2n OTf
N
N
n
b
Cu-12
Cu
FE$_{ethylene}$(%)
E (V vs RHE)
c
CO
C$_2$H$_4$
Cu-12
CO
C$_2$H$_4$
Cu
FE (%)
E (V vs RHE)

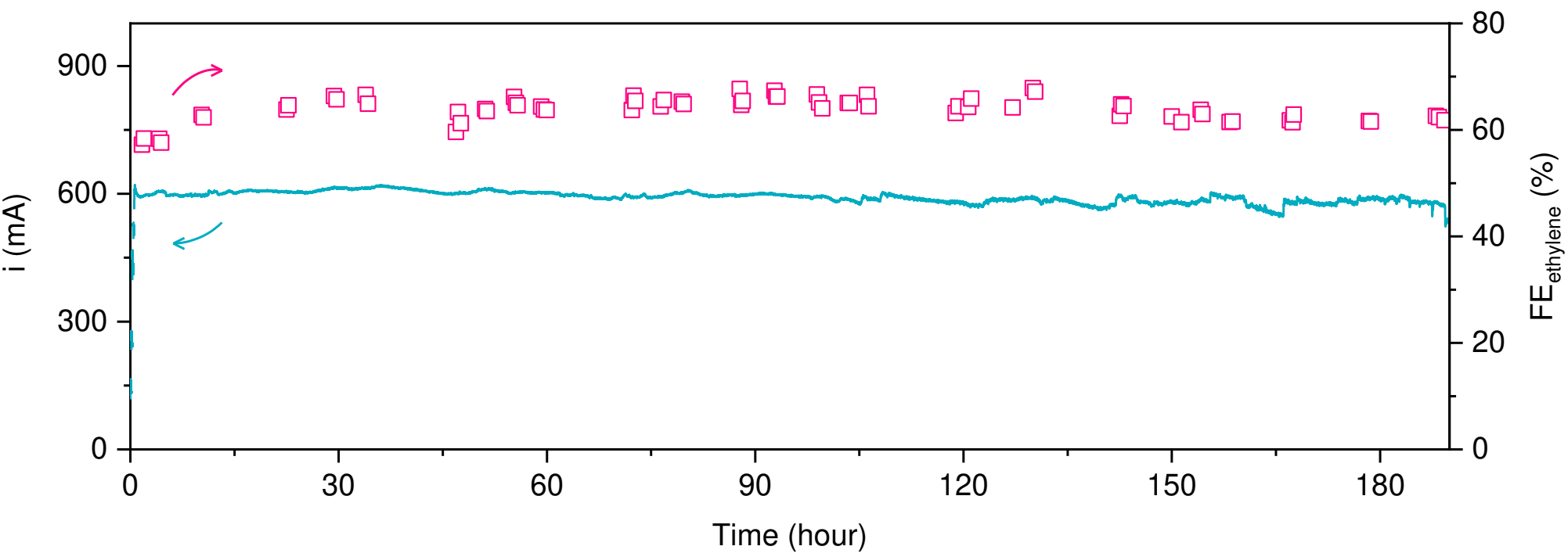
900
600
300
0
i (mA)
80
60
40
20
0
FE ethylene (%)
0
30
60
90
120
150
180
Time (hour)